Supplementary Information

Phase-pure antiferroelectric $AgNbO_3$ films on Si substrates: chemical solution deposition and phase transitions

Liang Shu[a], *Xin Zhang*[a], *Wei Li*[a], *Jing Gao*[a], *Hongliang Wang*[a], *Yu Huang*[a], *Yue-Yu-Shan Cheng*[a], *Qian Li*[a,*], *Lisha Liu*[a,*] *and Jing-Feng Li*[a,*]

[a] State Key Laboratory of New Ceramics and Fine Processing, School of Materials Science and Engineering, Tsinghua University, 100084, Beijing, China.

*Corresponding author.
E-mail:
Jing-Feng Li: jingfeng@mail.tsinghua.edu.cn
Lisha Liu: net4663@126.com
Qian Li: qianli_mse@tsinghua.edu.cn

1. The evidence of hypothesis stabilization mechanism

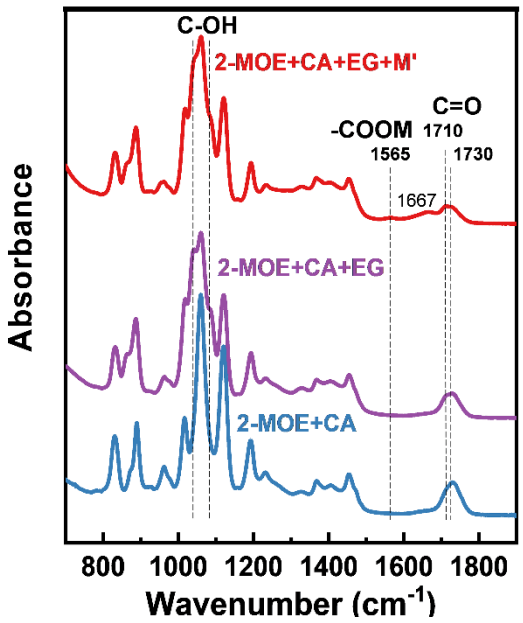

Fig. S1 Fourier transform infrared (FTIR) spectroscopy of (a) 2-MOE+CA solution; (b) 2-MOE+CA+EG solution; (c) 2-MOE+CA+EG+M' solution, where M' denotes metal salt or metal alkoxide, here meaning $AgNO_3$ and $Nb(OCH_2CH_3)_5$.

FT-IR spectroscopy has been considered to be one of the powerful spectroscopic tool for the detemination of funcational groups in the organic solution to study and understand the reaction machanisms.[1] We designed three groups of solutions : "2-MOE+CA" group as control group, "2-MOE+CA+EG" as the experimental group to investigate the esterification reaction between EG and CA, and "2-MOE+CA+EG+M' " as the other experimental group to confirm the chelating reaction between metal ions with CA. As shown in **Fig. S1**, in "2-MOE+CA" solution, the characteristic peak at 1730 cm^{-1} has been assigned to carbonyl C=O stretching mode in the -COOH carboxylic-acid groups of CA. The shoulder peak at 1710 cm^{-1} around the C=O peak (1730 cm^{-1}) results from the reaction between the -COOH in CA and -OH in 2-MOE. After introducing EG in the "2-MOE+CA" solution, the intensity of the shoulder peak at 1710 cm^{-1} becomes more stronger, accompanied by the additional characteristic peaks for C-OH mode between 1000 cm^{-1} and 1100 cm^{-1}, suggesting the more esterification reaction happens between -OH in EG and -COOH in CA to form the organic network. With further adding metal salt or metal alkoxide (M', denoting $AgNO_3$ and $Nb(OCH_2CH_3)_5$) in "2-MOE+CA+EG" solution, the absorbance peak at 1565 cm^{-1} characterized by the -COOM group evidences the chelating effect of -COOH in CA. Meanwhile, the peak occurring at 1667 cm^{-1} denotes the formation of R-NO_2, indicating the incorporation of NO_3^- in $AgNO_3$ into the organic network.

2. Texture discussion

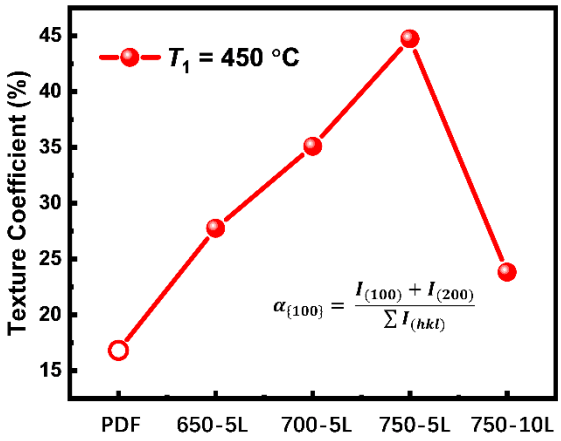

Fig. S2 The annealing temperature and thickness dependence of (100) texture coefficient of 5-layer $AgNbO_3$ films pyrolyzed at 450 °C compared with PDF card of $AgNbO_3$ (JCPDS file No. 70-4738)

For CSD, film texturing is often observed depending on the annealing temperature and substrate.[1–5] Here, in 5-layer $AgNbO_3$ films pyrolyzed at 450 °C, {100} texturing development (here the orientation of (200) dominates) is observed with increasing annealing temperature. The texture coefficient is calculated from the peak intensity using the following equation:

$$\alpha_{\{100\}} = \frac{I_{(100)}+I_{(200)}}{\sum I_{(hkl)}} \quad (1)$$

where α denotes the texture coefficient, *I* represents the integration intensity of XRD peaks of $AgNbO_3$ phase, and the subscripts denote the peak index. The texture coefficient is significantly increased from 28% to 45% as the annealing temperature increases from 650 °C to 750 °C, suggesting higher annealing temperature promotes heterogeneous nucleation and grain growth of $AgNbO_3$ (200) on the surface of $Pt/Ti/SiO_2/Si$ substrate. With further increasing the film thickness (i.e., 10-layer films annealing at 750 °C), heterogeneous nucleation of $AgNbO_3$ (200) is reduced which can be seen from the significantly decreased texture coefficient to 24% in 10-layer $AgNbO_3$ films, as shown in the **Fig. S2**, indicating the heterogenous nucleation gradually turns to homogenous nucleation due to reduced heterogeneous interface effect.

3. Raman spectrum for determining oxygen vacancies

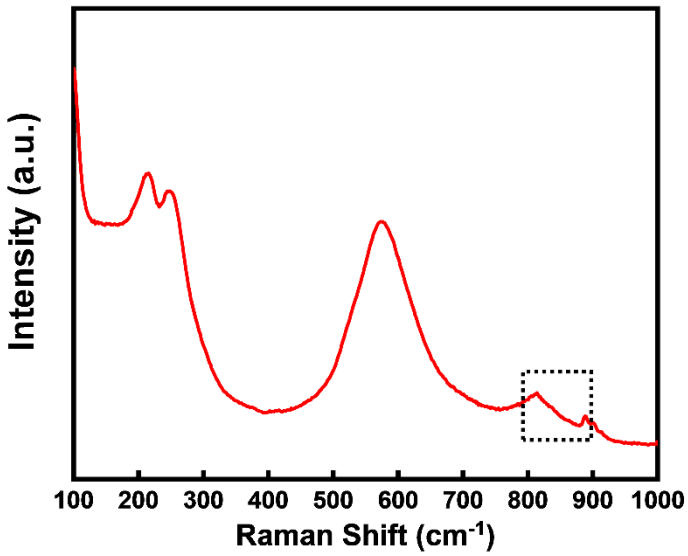

Fig. S3 Room-temperature Raman shift of the as-prepared 10-layer $AgNbO_3$ film ranging from 100 cm^{-1} to 1000 cm^{-1}

The oxygen vacancies have also been characterized by Raman spectra, where the peak around 828 cm^{-1} is the signal for adsorbed oxygen species at the surface.[6–9] Additionally, for perovskite structure, there is an extra strong peak at 890 cm^{-1}, reflecting the existence of more oxygen vacancies for the as-prepared $AgNbO_3$ films, corresponding to the XPS fitting.

4. Quantitative EDS results

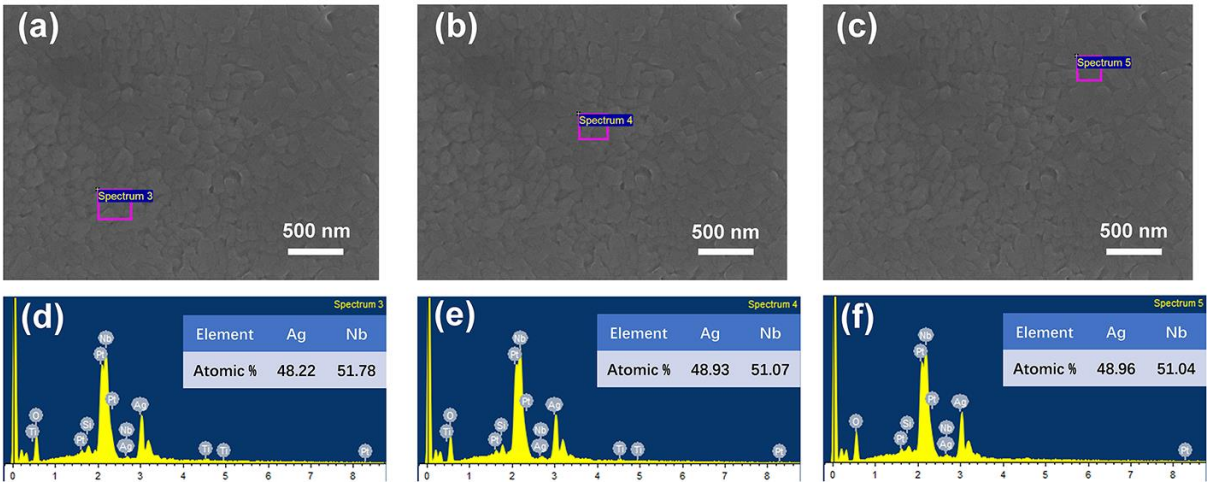

Fig. S4 (a)-(c) SEM images with different selected areas (purple rectangular) for element quantitative analysis; (d)-(f) quantitative EDS results of the as-prepared 10-layer $AgNbO_3$ film corresponding to the selected areas.

5. Temperature-dependent XRD measurement

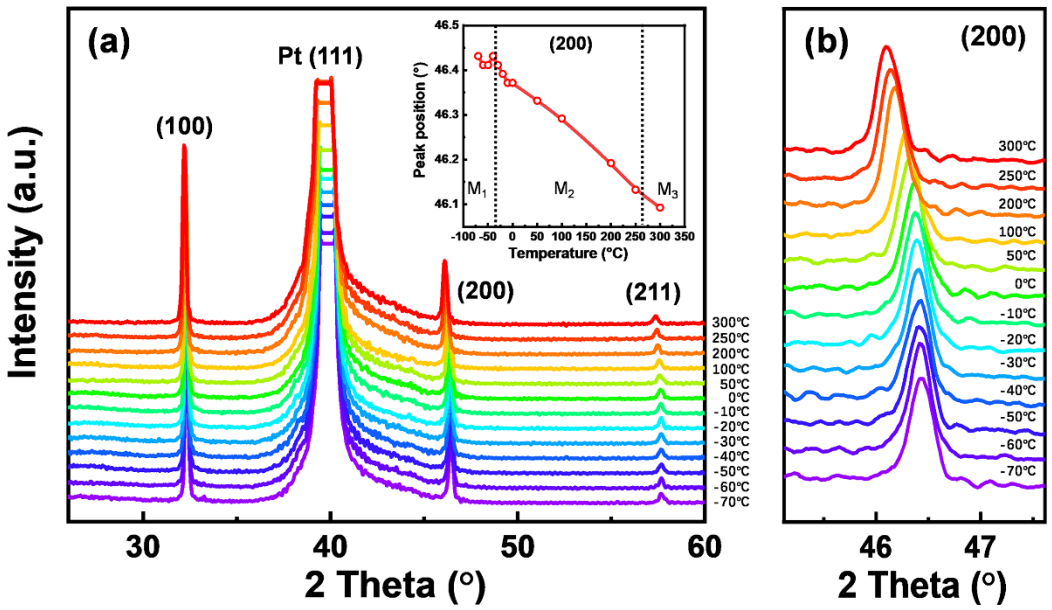

Fig. S5 (a) The temperature-dependent XRD patterns of the phase-pure $AgNbO_3$ film from -70 °C to 300 °C; the inset: the peak position of $AgNbO_3$ (200) as a function of temperature. (b) The enlarged figure of $AgNbO_3$ (200) peak as a function of temperature.

The temperature-dependent XRD analysis has been also conducted to investigate phase transition between M (M_1, M_2, and M_3) phases from -70 °C to 300 °C under N_2 atomosphere, where no secondary phases have been detected as shown in **Fig S5 (a)**. The enlarged (200) peaks in **Fig. S5(b)** shows obvious peak shifting towards a lower angle with increasing temperature, suggesting the tendency of the increased lattice parameter along *c* axis. Howerer, there is an anomaly between -50 °C to -25 °C as shown in the inset of **Fig. S5 (a)**, corresponding to the phase transition temperature range of M_1-M_2 determined by temperature-dependent dielectric permittivity in **Fig. 5(b)**. This indicates that the lattice parameter along c axis first has a sudden decrease and then increases when entering M_2 phase from M_1, which may be due to the change of space group symmetry (probably from $Pmc2_1$ and Pbcm) between the two phases. Such lattice parameter changing behavior can also be observed in Li doped $AgNbO_3$ ceramics during the transition between two polar phases ($P2_1am$/R3c) to the antiferroelctric Pbnm phase.[10] For comparison, relatively smaller change asscociated with the proposed M_2 and M_3 transition suggests less difference between the phase structure of M_2 and M_3.

6. Temperature-insensitive dielectric permittivity with low loss

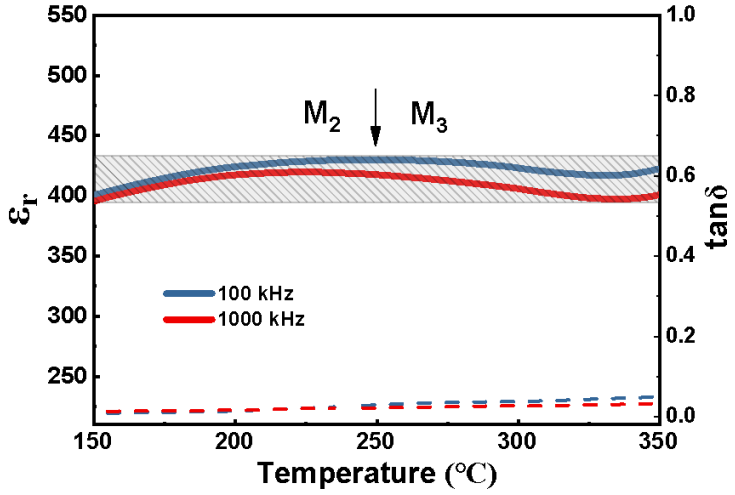

Fig. S6 The temperature-dependent dielectric permittivity and loss of the phase-pure $AgNbO_3$ films from 150 °C to 350 °C measured at 100 kHz and 1 MHz.

Table S1 The dielectric properties of the as-prepared $AgNbO_3$ films compared with other $Ag(Nb,Ta)O_3$ films measured at 100 kHz at both higher temperature (HT) and room temperature (RT).

Film	Substrate	ε_r (High T)	tanδ (High T)	ε_r (RT)	tanδ (RT)	Ref
(00*l*) $Ag(Nb_{0.5}Ta_{0.5})O_3$	(001)SRO/LAO	275±25 (150~290 °C)	0.025~0.037	357	0.020	11,12
(00*l*)$Ag_2(Nb_{0.5}Ta_{0.5})_4O_{11}$	(111)Pt/Ti/SiO_2/Si	104±1 (150~200 °C)	0.021~0.037	118	0.004	13
* $Ag(Nb_{0.5}Ta_{0.5})O_3$	(111)Pt/Ti/SiO_2/Si	210±8 (150~200 °C)	0.028~0.043	250	0.004	13
$AgNbO_3$ (100 kHz)	(111)Pt/Ti/SiO_2/Si	416±14 (150~350 °C)	0.006~0.042	315	0.020	This Work
$AgNbO_3$ (1 MHz)	(111)Pt/Ti/SiO_2/Si	408±12 (150~350 °C)	0.008~0.032	312	0.015	This Work

* Mostly perovskite $Ag(Nb_{0.5}Ta_{0.5})O_3$ with little natrotantite secondary phase

7. Seebeck coeffient measurement

Fig. S7 The Seebeck coeffient testment results of the film surface at 400 °C

Seebeck coefficient was tested by portable Seebeck tester (PTM-3, JouleYacht, China) at 400 °C on the hot plate with probes contacting the surface of films. As shown in the **Fig. S7**, the nagtive Seebeck coefficients are shown after testing for three times at different places, indicating that the main excited carriers are electrons. Therefore, we reasonably infer that the free carrier of the film is the electron.

8. Cross-section EDS maping in TEM mode

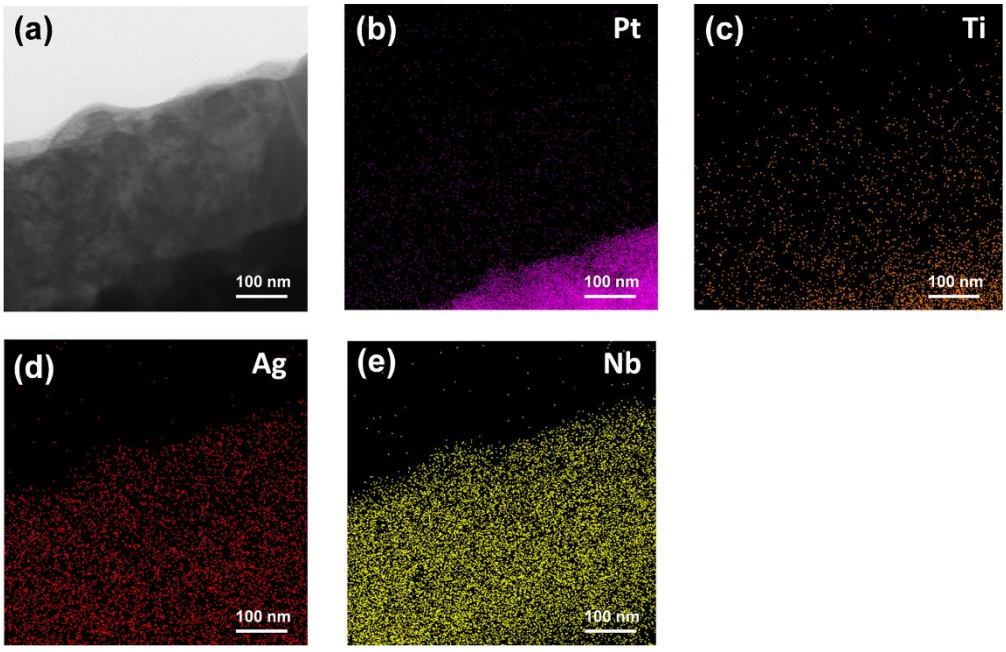

Fig. S8 (a) The bight-field TEM image of the cross-section of film and substrat (b)-(e) EDS mapping results of elements of Pt, Ti, Ag and Nb, respectively.

References

1 Y. Wang, H. Cheng, J. Yan, N. Chen, P. Yan, F. Yang and J. Ouyang, *Materialia*, 2019, **5**, 100228.

2 H. Zhu, Y.-Y. Zhao, J. Ouyang, K. Wang, H. Cheng and Y. Su, *ACS Appl. Mater. Interfaces*, 2022, **14**, 7805–7813.

3 Z. Zhou, S. Zhang, Y. Zhang, J. Luo, W. Sun, X. Wang and J. Li, *Adv. Electron. Mater.*, 2018, **4**, 1800351.

4 S. Zhang, J. Luo, Z. Zhou and J. Li, *J. Am. Ceram. Soc.*, 2018, **102**, 2696.

5 L. Liu, X. Qiu, S. Zhang, Z. Zhou, Y. Huang, L. Shu, Y. Cheng, X. Wang and J. Li, *J. Am. Ceram. Soc.*, 2020, **103**, 6554–6564.

6 H. Trabelsi, M. Bejar, E. Dhahri, M. P. F. Graça, M. A. Valente, M. J. Soares and N. A. Sobolev, *Appl. Surf. Sci.*, 2017, **426**, 386–390.

7 Q. Ji, L. Bi, J. Zhang, H. Cao and X. S. Zhao, *Energy Environ. Sci.*, 2020, **13**, 1408–1428.

8 A. Benali, M. Bejar, E. Dhahri, M. Sajieddine, M. P. F. Graça and M. A. Valente, *Mater. Chem. Phys.*, 2015, **149–150**, 467–472.

9 D. Chapron, F. Cordero and M. D. Fontana, *J. Appl. Phys.*, 2019, **126**, 154101.

10 U. Farid, A. S. Gibbs and B. J. Kennedy, *Inorg. Chem.*, 2020, **59**, 12595–12607.

11 M. B. Telli, S. S. N. Bharadwaja, M. D. Biegalski, J. G. Cheng and S. Trolier-McKinstry, *J. Appl. Phys.*, 2007, **101**, 014111.

12 R. L. Johnson-Wilke, R. H. T. Wilke, C. B. Yeager, D. S. Tinberg, I. M. Reaney, I. Levin, D. D. Fong and S. Trolier-McKinstry, *J. Appl. Phys.*, 2015, **117**, 085309.

13 M. B. Telli, S. Trolier-McKinstry, D. I. Woodward and I. M. Reaney, *J. Sol-Gel Sci. Technol.*, 2007, **42**, 407–414.